

Full length article

Laser pulse heating of steel mixing with WC particles in a irradiated region

S.Z. Shuja^a, B.S. Yilbas^{a,*}, H. Ali^a, C. Karatas^b^a ME Department, King Fahd University of Petroleum & Minerals, Dhahran, Saudi Arabia^b Engineering Faculty, Hacettepe University, Ankara, Turkey

ARTICLE INFO

Article history:

Received 20 April 2016

Received in revised form

28 June 2016

Accepted 25 July 2016

Available online 31 July 2016

Keywords:

Laser pulse heating

WC particles

Steel

Temperature field

ABSTRACT

Laser pulse heating of steel mixing with tungsten carbide (WC) particles is carried out. Temperature field in the irradiated region is simulated in line with the experimental conditions. In the analysis, a laser pulse parameter is introduced, which defines the laser pulse intensity distribution at the irradiated surface. The influence of the laser parameter on the melt pool size and the maximum temperature increase in the irradiated region is examined. Surface temperature predictions are compared with the experimental data. In addition, the distribution of WC particles and their re-locations in the treated layer, due to combination of the natural convection and Marangoni currents, are predicted. The findings are compared to the experimental data. It is found that surface temperature predictions agree well with the experimental data. The dislocated WC particles form a streamlining in the near region of the melt pool wall, which agree with the experimental findings. The Gaussian distribution of the laser pulse intensity results in the maximum peak temperature and the maximum flow velocity inside the melt pool. In this case, the melt pool depth becomes the largest as compared to those corresponding to other laser pulse intensity distributions at the irradiated surface.

© 2016 Elsevier Ltd. All rights reserved.

1. Introduction

Laser sintering offers considerable advantages over the conventional methods because of precision of operation, short processing time, local treatment, and low cost. In laser sintering process, high power lasers are used and the irradiated surface undergoes the melting during the heating cycle of the treatment. In order to achieve high power intensity at the surface and control the phase change process in the irradiated region, laser repetitive pulses are favorable during the processing. Laser beam intensity distribution is, in general, Gaussian at the irradiated surface, which gives rise to attainment of the peak power intensity at the irradiated spot center. This in turn causes local evaporation of the surface where the peak intensity is high. To avoid excessive evaporation of the surface during the laser sintering, the laser power setting and overlapping of the irradiated spots at the surface needs to be precisely controlled. In addition, excessive heating at the surface causes melt over flow and formation of high temperature gradients in the surface region. Excess melt flow results in poor surface roughness and high temperature gradient while causing thermal stress formations in the treated region. This lowers quality

of sintering and limits the practical applications of the resulting end product. Although proper selection of laser sintering parameters is possible through the experimental data, it requires extensive efforts to finalize the selection process. In addition, laser pulse heating involves with localized temperature rise in a short duration; therefore, experimental study for the laser heating process becomes expensive because of the requirements of the state-of-the-art equipment. On the other hand, simulation studies provide physical insight of the processes, which take place during the laser-workpiece interaction. However, due to the limitations in computational power, the assumptions need to be made describing the physical process. Consequently, a care must be taken to describe accurately the laser interaction process in terms of modeling while incorporating some useful and necessary assumptions to reduce the computational efforts and the cost.

Considerable research studies were carried out to examine laser heating process with presence of particles. Laser heating of dust clusters was investigated by Thomsen et al. [1]. They showed that the laser scanning pattern had a major influence on both the velocity distribution function and the stationary structure of the clusters. Furthermore, the heating effect was found to be enhanced when the laser spots move with slightly higher frequencies than the trap frequency. Investigation of multi-component powder in selective laser sintering was carried out by Zhang et al. [2]. They indicated that with the increase of scanning time, the overall

* Corresponding author.

E-mail address: bsyilbas@kfupm.edu.sa (B.S. Yilbas).

Nomenclature

a	Gaussian parameter
C_p	specific heat at constant pressure (J/kg K)
E	volumetric energy gain (J/m ³)
h	enthalpy (J/kg)
h_t	heat transfer coefficient at the free surface (W/m ² K)
ΔH	enthalpy increase (J/kg)
k	thermal conductivity (W/m K)
L	latent heat of melting (J/kg)
r	radial direction (r – axis, m)
r_f	surface reflectivity
S_o	volumetric heat source (W/m ³)
T	temperature (K)
T_o	ambient temperature (K)
t	time (s)
u	velocity in the radial direction (m/s)

v	velocity in the axial direction (m/s)
\vec{v}_{liq}	liquid front velocity (m/s)
I_o	laser peak intensity (W/m ²)
p	pressure (Pa)
z	axial direction (z – axis, m)

Greek symbols

a	thermal diffusivity of the molten material (m ² /s)
β	laser pulse parameter
β_E	volumetric thermal expansion coefficient (1/K)
β_f	liquid fraction
δ	absorption coefficient (1/m)
ρ	density of material (kg/m ³)
σ_T	temperature coefficient of surface tension (N/m K)

temperature of the substrate and the particles was gradually rising; in which case, the heat-affected zone was increasing and the asymmetric temperature distribution became visible in the laser irradiated layer. Laser short-pulse heating and influence of spatial distribution of absorption coefficient on temperature field was examined in silicon film by Mansoor and Yilbas [3]. The findings revealed that electron temperature attained the highest for the case of high absorption coefficient located in the surface region of the silicon film. As the high absorption region moved inside the film, electron and lattice temperatures became low. Investigation of effect of gas flow and powder transport on laser direct metal deposition process was carried out by Kovalev et al. [4]. They demonstrated that the particles might overheat in between the nozzle and substrate; the overheating depended on the trajectories by which particles moved, on their size, and time of their retention in the laser-irradiation region. Analytical model for the geometrical characteristics of the laser sintered surfaces was introduced by Ioannou et al. [5]. They formulate the heating problem under the assumption that the maximum temperature remained below the melting point in the irradiated region and the energy lost due to conduction in the metal substrate was very small. Laser induced metallurgical changes in the re-solidified zone of W-Cu composite powder system was studied by Dai et al. [6]. They demonstrated that as the angle of attractive force and pressure was acute angle, tungsten particles formed a small-scaled rim structure and the rearrangement rate was limited, accordingly tending to form segregation structure. Otherwise, tungsten particles formed large-scale rim structure and the re-arrangement was efficient, contributing to the formation of homogeneously distributed structure. The thermal history of the multiple laser deposited layers was examined by Amine et al. [7]. They simplified the heating problem after assuming that the deposit geometry was known prior to the simulations; this would affect the temperature and stress fields developed during heating cycle. Thermal transport during coaxial laser direct deposition process was investigated by Wen and Shin [8]. In the model study, they introduced mass source term into the continuity equation, which considered the rate of the gas phase being replaced by the deposited material due to the moving interface during the phase change process. The study on laser melting of stainless steel 316L metal powders was carried out by Antony et al. [9]. They presented the effect of process parameters such as laser power, scanning speed, and beam size on the characteristics of the melt zone geometry and ball formation. Laser treatment of dual matrix cast iron with presence of WC particles at the surface was studied by

Yilbas et al. [10]. They showed that laser treated layer consisted of a dense region composing of fine grains and WC particles, and then followed dendritic and featherlike structures below the dense layer and the heat affected zone. Low temperature nanoparticle sintering was carried out by Kumpulainen et al. [11]. They indicated that laser sintering enabled short sintering times and selective sintering, which made it possible to avoid printed structures containing fragile active components. Effects of post-heat treatment on microstructure and properties of laser clad composite coatings on titanium alloy were examined by Li et al. [12]. They demonstrated that the post-heat treatment could decrease the residual stress and increased the fracture toughness of the coatings. High power direct diode laser cladding was investigated by Liu et al. [13]. They introduced an optical monitoring system consisting of a high-speed CCD camera, a pyrometer, and an infrared camera to analyze the mass and heat transfer in the cladding section.

Although laser interaction of surfaces was studied earlier [10], the main focus was to examine metallurgical changes in the laser treated region, and temperature field and particle distribution in the irradiated region were left for the future study. In the present study, laser heating of solid surface with presence of hard particles (WC) in the irradiated region is considered. Temperature distribution and particle dynamics in the melt are studied numerically. The findings of the particle distribution are compared with the experimental data. In the numerical simulations, phase change and melt flow in the irradiated region is incorporated and the absorption of the laser beam is modeled using the Lambert's law. The boundary conditions of the solution domain are set according to the experimental conditions. The study is extended to include the effect of laser pulse intensity distribution at the irradiated spot center on temperature field in the irradiated region. Laser pulse parameter is defined as β , which describes the exponential distribution of the pulse intensity at the surface. In this case, $\beta=0$ corresponds to Gaussian intensity distribution at the irradiated surface.

2. Heating analysis

Laser pulse heating of steel mixing with WC particles is considered. The heat transfer equation in relation to the laser pulse heating process can be written as:

$$\frac{DE}{Dt} = (\nabla(k\nabla T)) + S_o \quad (1)$$

where E is the energy gain per unit volume by the substrate material, k is the thermal conductivity, and S_o is the volumetric heat source term and it is:

$$S_o = I_0 \delta (1 - r_f) \exp(-\delta z) \exp\left(-\left(\frac{r}{a} + \beta\right)^2\right) f(t) \quad (2)$$

I_0 is laser peak intensity, δ is the absorption coefficient, a is the Gaussian parameter, r_f is the surface reflectivity, β is the laser pulse parameter, and r and z are the axes while the laser beam is located normal to the z -axis, i.e. the laser beam axis is the z -axis (Fig. 1). Fig. 2 shows normalized laser intensity distribution along the r -axis for various values of the laser pulse parameter.

The rate of energy gain by the substrate material yields:

$$\frac{DE}{Dt} = \frac{\partial(\rho C_p T)}{\partial t} \quad (3)$$

Combining Eqs. (1) and (3) yields:

$$\frac{\partial(\rho C_p T)}{\partial t} = (\nabla(k\nabla T)) + S_o \quad (4)$$

Eq. (4) is solved numerically with the appropriate boundary conditions to predict the temperature field in the substrate material. However, to analyze the phase change problem, the enthalpy-porosity technique is used. In this case, the melt interface is tracked explicitly after defining a quantity called the liquid fraction, which indicates the fraction of the cell volume that is in

liquid form. Based on the enthalpy balance, the liquid fraction is computed. The mushy zone is a region in which the liquid fraction lies between 0 and 1. The mushy zone is modeled as a “pseudo” porous medium in which the porosity decreases from 1 to 0 as the material solidifies. When the material has fully solidified in a cell, the porosity becomes zero and hence the velocities also drop to zero.

The enthalpy of the material is computed as the sum of the sensible enthalpy, h , and the latent heat, ΔH :

$$H = h + \Delta H \quad (5)$$

where

$$h = h_{ref} + \int_{T_{ref}}^T c_p dT \quad (6)$$

and

h_{ref} = reference enthalpy

T_{ref} = reference temperature

c_p = specific heat at constant pressure

The liquid fraction, β_f , can be defined as:

$\beta_f = 0$ if $T < T_{solidus}$

$\beta_f = 1$ if $T > T_{liquidus}$

$$\beta_f = \frac{T - T_{solidus}}{T_{liquidus} - T_{solidus}} \quad \text{if } T_{solidus} < T < T_{liquidus} \quad (7)$$

The latent heat content can now be written in terms of the latent heat of the material, L :

$$\Delta H = \beta_f L \quad (8)$$

The latent heat content can vary between zero (for a solid) and L (for a liquid). The enthalpy-porosity technique treats the mushy region (partially solidified region) as a porous medium. The porosity in each cell is set equal to the liquid fraction in that cell. In fully solidified regions, the porosity is equal to zero, which extinguishes the velocities in these regions. The momentum sink due to the reduced porosity in the mushy zone takes the following form:

$$S = \frac{(1 - \beta_f)^2}{(\beta_f^3 + \varepsilon)} A_{mush} (\vec{v}) \quad (9)$$

where β_f is the liquid fraction, ε is a small number (0.001) to prevent division by zero, A_{mush} is the mushy zone constant. The mushy zone constant measures the amplitude of the damping; the higher this value, the steeper the transition of the velocity of the material to zero as it solidifies. The liquid velocity can be found from the average velocity is determined from:

$$\vec{v}_{liq} = \frac{\vec{v}}{\beta_f} \quad (10)$$

The solution for temperature is essentially iteration between the energy equation (Eq. (4)) and the liquid fraction equation (Eq. (7)). Directly using Eq. (7) to update the liquid fraction usually results in poor convergence of the energy equation. However, the method suggested by Voller and Prakash [14] is used to update the liquid fraction based on the specific heat.

In order to solve Eq. (4), two boundary conditions for each principal axis should be specified. Due to the shielding gas, the convective boundary is assumed at the surface and constant temperature is considered at a distance considerably away from the surface (at the thickness). Since the depth of liquid region is significantly less than the thickness of the workpiece, the problem can be considered as the semi-infinite-body and this assumption simplifies the solution of the problem. The boundary conditions,

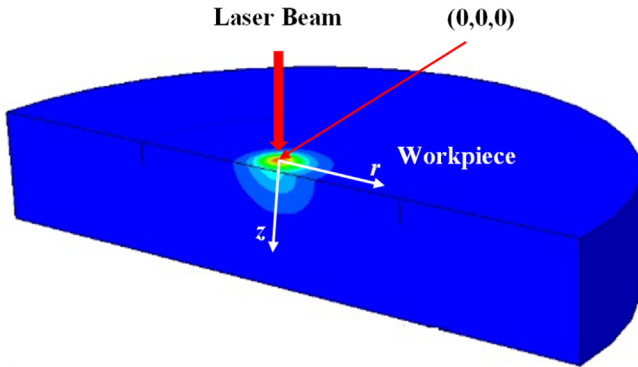


Fig. 1. A schematic view of laser heating situation.

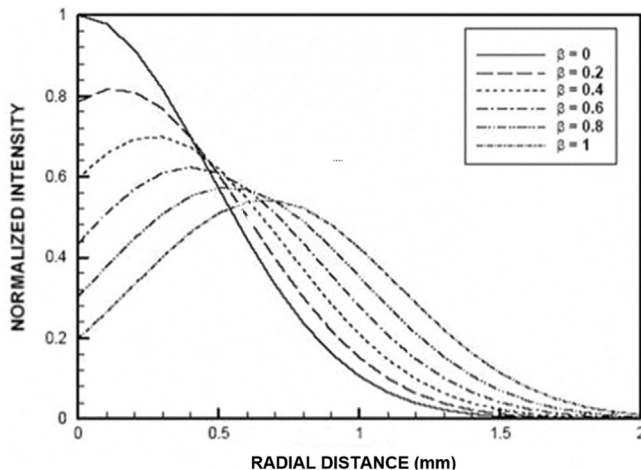


Fig. 2. Laser pulse intensity distribution in the radial direction at the surface for various laser pulse parameter (β).

therefore, are:

z at the thickness (z_{th}) $\Rightarrow z = z_{th}$: $T(r, \infty, t) = T_0$ (specified)

r at infinity $\Rightarrow r = \infty$: $T(\infty, z, t) = T_0$ (specified)

At symmetry axis $\Rightarrow r = 0$: $\frac{\partial T(0, z, t)}{\partial r} = 0$

At the surface $\Rightarrow z = 0$: $k \frac{\partial T(r, 0, t)}{\partial z} = h_t(T_s - T_\infty)$ where h is the heat transfer coefficient at the free surface. The heat transfer coefficient predicted earlier [15] is used in the present simulations ($h_t = 10^4$ W/m² K).

The continuity and momentum equations in the melt layer are different than that corresponding to the mushy zone. Therefore, the conservation equations need to be incorporated to account for the flow field. This problem is governed by the axisymmetric Navier-Stokes equation. For laminar flow, the conservation equations are:

$$\text{Continuity} \quad \frac{\partial u}{\partial z} + \frac{1}{r} \frac{\partial(rv)}{\partial r} = 0$$

$$r - \text{dir} \quad \frac{\partial v}{\partial t} + u \frac{\partial v}{\partial z} + v \frac{\partial v}{\partial r} \\ = - \frac{1}{\rho} \frac{\partial p}{\partial r} + \mu \left(\frac{\partial^2 v}{\partial z^2} + \frac{1}{r} \frac{\partial}{\partial r} \left(r \frac{\partial v}{\partial r} \right) - \frac{v}{r^2} \right)$$

$$z - \text{dir} \quad \frac{\partial u}{\partial t} + u \frac{\partial u}{\partial z} + v \frac{\partial u}{\partial r} \\ = - \frac{1}{\rho} \frac{\partial p}{\partial z} + \mu \left(\frac{\partial^2 u}{\partial z^2} + \frac{1}{r} \frac{\partial}{\partial r} \left(r \frac{\partial u}{\partial r} \right) \right) + g\beta_E T + S_z$$

$$\text{Energy} \quad \rho \frac{\partial(H)}{\partial t} + \nabla \cdot (\rho \bar{v}H) = \nabla \cdot (k \nabla T) + S_o - S_h$$

or

$$\frac{\partial T}{\partial t} + u \frac{\partial T}{\partial z} + v \frac{\partial T}{\partial r} = \alpha \left(\frac{\partial^2 T}{\partial z^2} + \frac{1}{r} \frac{\partial}{\partial r} \left(r \frac{\partial T}{\partial r} \right) \right) + S_o - S_h \quad (11)$$

where u and v are the component of the velocity in the radial r and axial z directions, respectively, p is the pressure, T is the temperature, α is the thermal diffusivity of the molten material, β_E is the volumetric thermal expansion coefficient, which is formulated using the Boussinesq approximation, S_z is the momentum sink due to the reduced porosity in the mushy zone (Eq. (8)), and S_h is a phase related source term convection-diffusion phase change ($S_h = \frac{\partial(\rho \Delta H_s)}{\partial t} + \nabla \cdot (\rho \bar{v} \Delta H_s)$, where $\Delta H_s = H - \rho C_p T$) [14]. The term $g\beta_E T$ is the buoyancy term, which is used to introduce natural convection in the melt pool. The energy equation is similar to Eq. (4). Eq. (11) is used for the phase change and the liquid phase during the laser heating process. Moreover, a zero reference temperature has been assumed for the buoyancy force term in the z -direction momentum equation. Boundary conditions for Eq. (11) are as follows:

Free surface (at $z=0$)

$$\mu \frac{\partial v}{\partial z} = - \sigma_T \frac{\partial T}{\partial r} : u = 0 : -k \frac{\partial T}{\partial z} = q_{loss}$$

where q_{loss} includes the convective losses from the surface. The heat transfer coefficient is taken as $h_t = 10^4$ W/m² K at the surface [15].

Axis of symmetry (at $r=0$):

$$v = 0 : \frac{\partial u}{\partial r} = 0 : \frac{\partial T}{\partial r} = 0$$

Far field (solid):

$$T = T_0$$

where T_0 is the ambient temperature. The equation $\mu \frac{\partial v}{\partial z} = - \sigma_T \frac{\partial T}{\partial r}$ states the balance between the surface tension force and the viscous force on the free surface, where σ_T is the temperature coefficient of surface tension, which is a property of the material.

3. Numerical solution

To solve the governing equation of energy (Eq. (4)), finite element method is introduced. This method provides a means of spatial and temporal discretization of the governing equation. As a first step the application of the Galerkin method for the transient equation subjected to appropriate boundary and initial conditions is addressed. The calculation domain is divided into elements. The temperature is discretized over space as follows:

$$T(r, z, t) = \sum_{i=1}^n N_i(r, z) T_i(t) \quad (12)$$

where N_i are the shape functions, n is the number of nodes in an element, and $T_i(t)$ are the time-dependent nodal temperatures. Triangular elements are used, which defines the shape functions for the present study.

The Galerkin representation of the energy equation is:

$$\int_{\Omega} N_i \left[\nabla \cdot (k \nabla T) - \frac{\partial(\rho c_p T)}{\partial t} \right] d\Omega = 0 \quad (13)$$

Ω is the solution domain. Employing the Gauss-divergence theorem for the conduction term and on substituting the spatial approximation from Eq. (3), the spatially discretized finite element equation becomes:

$$[C] \left\{ \frac{\partial T}{\partial t} \right\} + [K] \{ T \} = \{ f \} \quad (14)$$

where

$$[C] = \int_{\Omega} \rho c_p [N]^T [N] d\Omega; \quad [K] = \int_{\Omega} [B]^T [D] [B] d\Omega; \\ \{ f \} = \int_{\Gamma_q} q [N]^T d\Gamma_q \quad (15)$$

Γ_q is the boundary where q the heat flux is prescribed. $[B] = \nabla N$ is the derivative matrix, which relates the gradient of the field variable to the nodal values, and $[D]$ is the property matrix.

The implicit scheme with a backward difference approximation (BDF) for the time used in the study is unconditionally stable; however, the accuracy of the scheme is governed by the size of the time step. A computer program based on implicit scheme is used to compute the temperature field. Table 1 gives the thermal properties of material used in the simulations. The laser power is kept the same as the experimental value in the simulations, i.e. Gaussian parameter $a = 2/3 \times R$ (R is a laser beam radius at the workpiece surface $R = 0.5$ mm) and power intensity $I_0 = 2.1 \times 10^8$ W/m².

Table 1

Material properties used in the simulations. The liquidus and solidus temperatures are $T_{liquidus} = 1448$ °C and $T_{solidus} = 1405$ °C. Melting temperature of WC is 2593 °C. Absorption coefficient (δ) = 6.17×10^7 1/m.

		Temp (K)	300	400	600	800	1000	1200	1500
Steel	Cp (J/Kg K)	477	515	557	582	611	640	682	
	K (W/m K)	14.9	16.6	19.8	22.6	25.4	28	31.7	
	ρ (kg/m ³)	8018	7968	7868	7769	7668	7568	7418	
Tungsten carbide	Cp (J/Kg K)	203							
	K (W/m K)	63							
	ρ (kg/m ³)	15,800							

4. Experimental

In line with the previous study [16], the workpieces were formed from steel mixing with 15% commercial-grade WC powders (Kennametal, USA). The workpieces were in a circular pellet form of 25.4 mm in diameter and 3 mm in thickness. Steel powders had particle size in the order of 50 μm and WC powders had median size of 5 μm . To prepare the pellets, WC and steel powders were mixed in isopropyl alcohol. The slurry was, then, ultrasonically shook to achieve homogeneity for 30 min. The pellets were compacted through sintering, hot-pressing, and hot isostatic pressing. The pellets were cold-pressed at 60 MPa, provided that the higher pressures resulted in undesirable striations in the compacts and they were sintered in a vacuum furnace at a temperature within the range of 910 °C in an environment pressure of 5×10^{-2} Pa for thirty minutes. Hot isostatic pressing were performed in accordance with the maximum temperature (1100 °C) for 30 min hold at 200 MPa argon environments. Heating and cooling rates of 50 °C/min were used at 200 MPa. The pellets were furnace cooled under the vacuum conditions. Fig. 3 shows the distribution of WC particles across the cross-section of the workpiece.

The CO₂ laser (LC-ALPHAIII) delivering a nominal output power of 2 kW was used to irradiate the workpiece surface. The nominal focal length of the focusing lens was 127 mm and the power intensity of the laser beam was Gaussian at the irradiated surface with the spot radius of ~ 1 mm. Nitrogen gas used as the shielding gas was applied co-axially with the laser beam using a conical nozzle and the laser treatment was repeated several times using different laser parameters. Laser parameters resulting in controlled melting of the surface with a minimum of surface defects, such as very small cavities without crack networks, were selected and the laser treatment conditions are given in Table 2. Material characterization of the laser treated surfaces was conducted using Jeol 6460 Scanning Electron Microscope (SEM). Fig. 4 shows X-ray diffractogram of laser treated surface. The presence of nitrogen gives rise to formation of Fe₂₋₃N and Fe₄N in the surface region. Table 3 gives the EDS data prior and after the laser treated workpieces. It is evident that elemental composition does not change significantly after the laser treatment process. Although quantification of nitrogen is involved with error in the EDS data, the presence of nitrogen indicates the formation of nitride compounds at the surface due to nitrogen gas assisted processing.

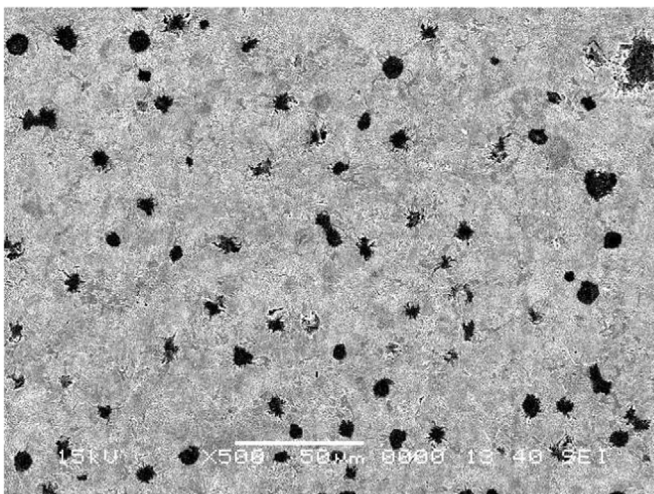


Fig. 3. SEM micrograph of workpiece cross-section prior to laser heating. The dark inclusions are WC particles.

Table 2

Laser pulse parameters used in the experiment and simulations.

I_0 (W/m ²)	a (mm)	Beam radius (mm)	Pulse length (s)	Shielding gas pressure (kPa)
2.1×10^8	1.33	2	5	500

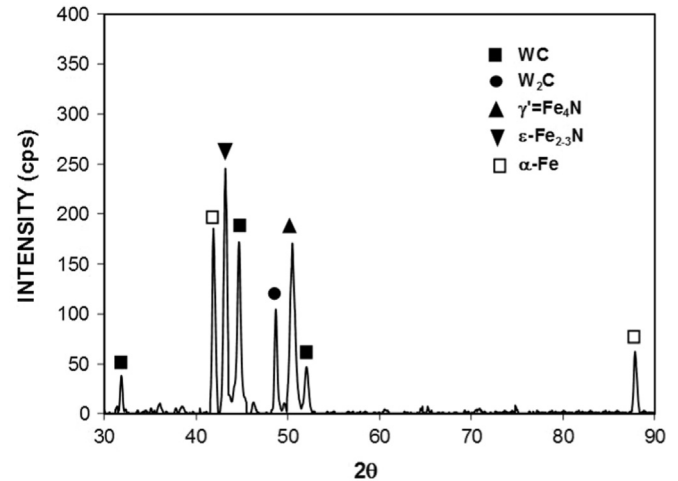


Fig. 4. X-ray diffractogram of laser treated surface.

Table 3

Elemental composition of as received and after the laser treatment of workpiece surface (wt%).

	WC	N	Fe
As received	15.1	0.0	Balance
Laser treated	14.3	6.2	Balance

5. Results and discussion

Laser melting of steel with presence of WC particles is considered. Temperature field and WC particle distribution are evaluated numerically in line with the experimental conditions. The influence of laser intensity distribution on the melting of the solid substrate is also presented.

Fig. 5 shows temperature contours in the heated layer for different values of the laser pulse parameter (β). It should be noted $\beta=0$ corresponds to the Gaussian beam profile at the irradiated surface. This can also be seen from Fig. 2, in which the laser pulse intensity variation along the radial direction is shown for various laser pulse parameters (β). Since the intensity distribution changes at the irradiated spot with the laser pulse parameter, temperature distribution and the peak temperature change in the irradiated zone with the laser pulse parameter. In this case, irradiated beam diameter, where the intensity remains high, increases as the pulse parameter increases. Since the total pulse energy is kept the same for all the laser pulse parameters, the peak power intensity reduces as the diameter of high beam intensity increases. This gives rise to a reduced peak temperature at the irradiated spot center and relatively large area of the heated surface. Although the peak temperature reduces at the irradiated spot center for large value of the laser pulse parameter, temperature difference along the radial direction becomes small in the central region of the irradiated spot. Therefore, the high peak intensity causes localized temperature increase in the irradiated spot center. In addition, exponential decay of the laser pulse intensity results in almost exponential decay of temperature across the irradiated spot surface. The depth of melted region remains higher for the Gaussian

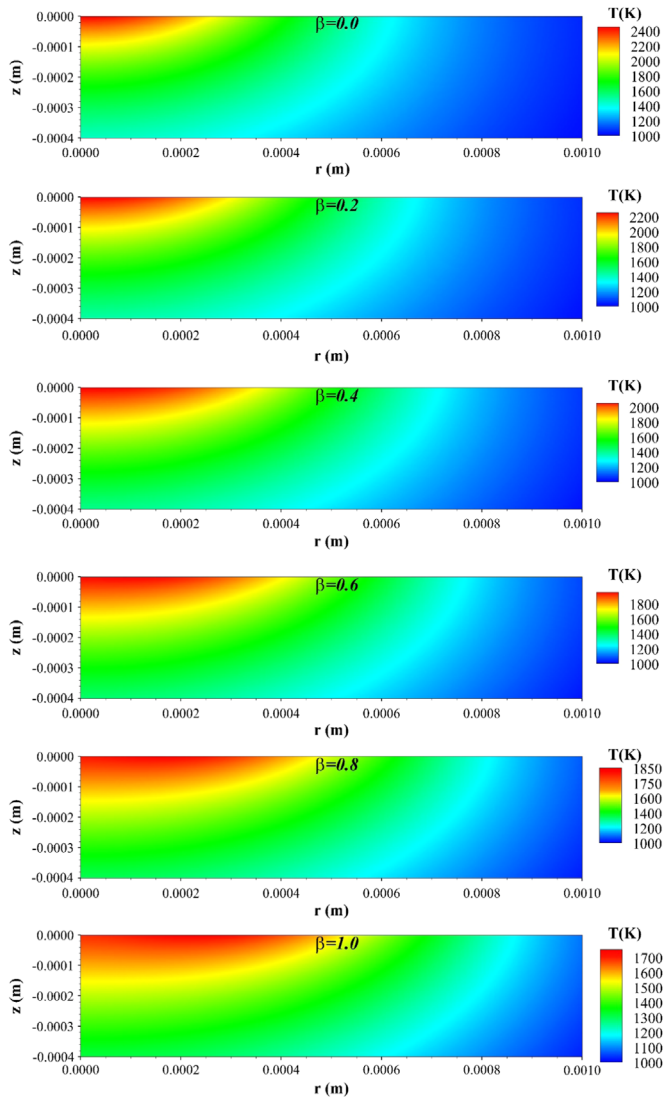


Fig. 5. Temperature contours in the cross-section of laser irradiated region for various values of laser pulse parameter.

intensity distribution ($\beta=0$) than the other distributions corresponding to the different values of the pulse parameter. This situation is seen from Fig. 6, in which the liquid layer formed in the heated region is shown for various values of the laser pulse parameter. Increasing pulse parameter reduces the melt depth; however, the melt size increases in the radial direction. Consequently, the large temperature gradient developed in the surface region of the irradiated surface enhances the heat diffusion from surface region towards the solid bulk. In addition, increased peak power intensity at the irradiated spot center for $\beta=0$ enhances the internal energy gain of the substrate material from the irradiated field. Consequently, increased heat diffusion from the surface region towards the solid bulk and internal energy gain from the irradiated field enhances the depth of the melt pool inside the substrate material. As the pulse parameter increases, the radial growth of the melt pool size increases because of the intensity distribution in the radial direction. However, increase in the melt pool depth as compared the melt pool diameter becomes small. Therefore, the ratio of the melt pool depth over the melt pool width decreases sharply with increasing laser pulse parameter. Moreover, for $\beta=1$, the melt pool depth becomes larger at some distance away from the symmetry axis than that corresponding to the symmetry axis. Therefore, the location of the peak intensity in

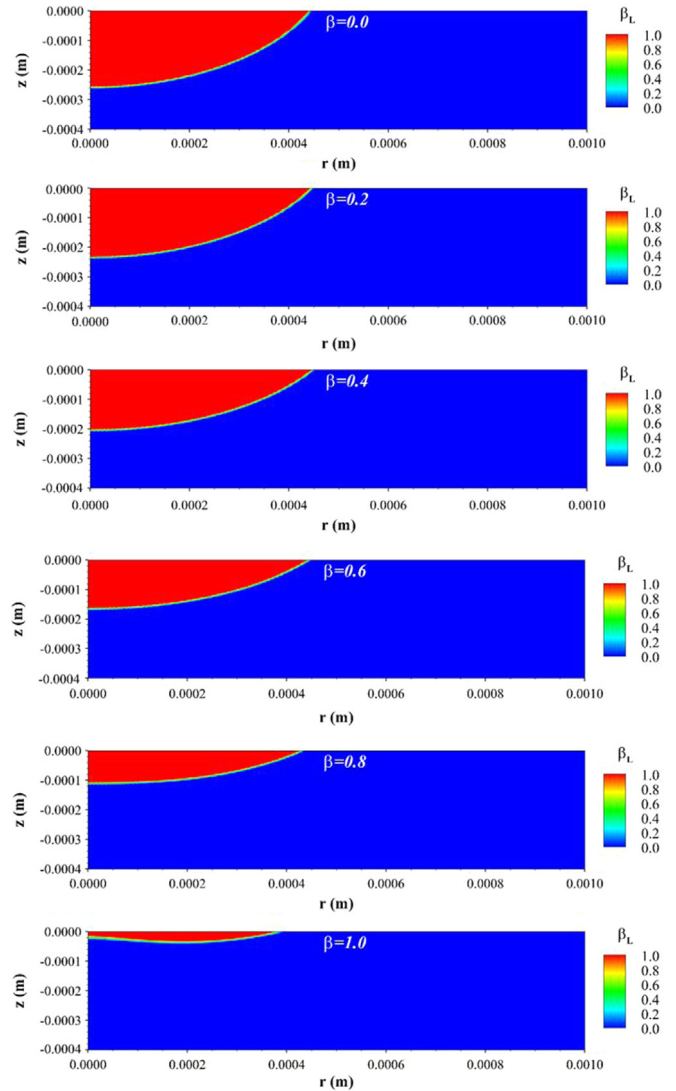


Fig. 6. Liquid fraction contours in the cross-section of laser irradiated region for various values of laser pulse parameter.

the radial direction is critical to achieve the desired melt pool size and the melt geometric configuration. In this case, locating of the peak intensity away from the symmetry axis at the irradiated surface can possibly provide almost uniform melt pool depth below the surface.

Fig. 7 shows the hard particle (WC) distribution in the melt zone after $t=0.5$ s of the melt zone formation for different values of the laser pulse parameter. Due to the natural convection and Marangoni currents formed, because of the density and surface tension variation, results in relocation of these particles in the melt pool. This situation can also be seen from Fig. 8, in which time variation of particle distribution in the melt pool is shown for the case of $\beta=0$. It should be noted that the melting temperature of WC is in the order of 2593 °C, they remain as solid in the melt pool. These particles form a streamline alignment in the melt pool because of the convection and Marangoni currents. Since the rate of fluid strain remains high in the close region of the melt pool wall, flow velocity remains low in this region. In this case, some of the hard particles appear to be relocated in this region because of relatively smaller inertia force generated by the natural convection current as compared to some regions away from the wall. In addition, the mobility of the particles remains low in the near region of the wall, which contributes to the attainment of more particles

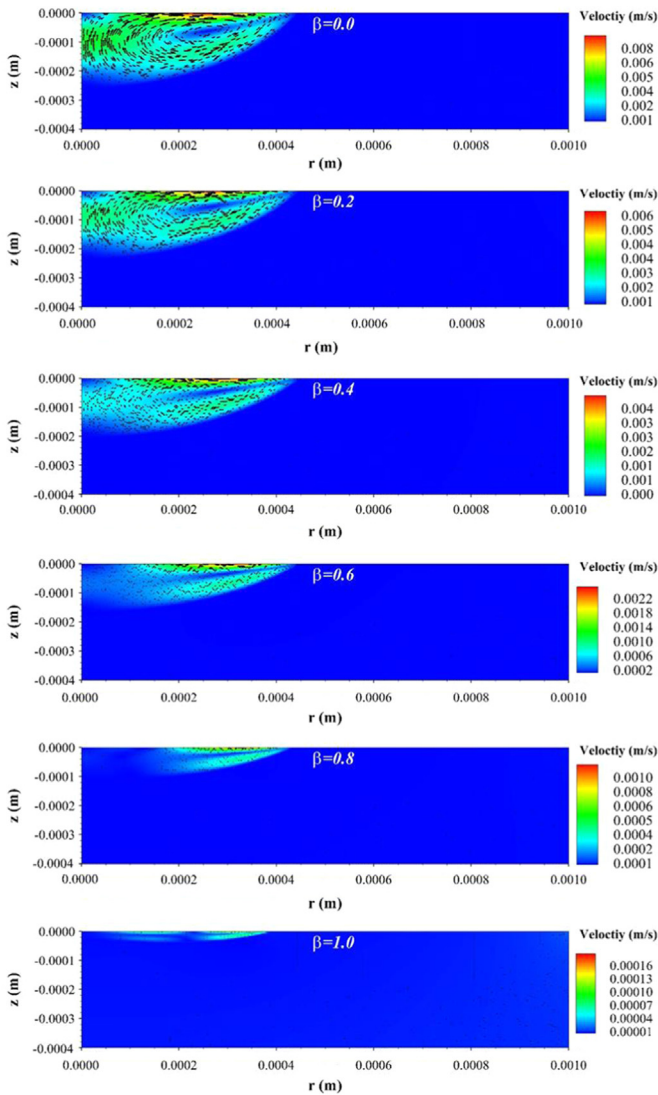


Fig. 7. WC particle distribution in the cross-section of laser irradiated region for various values of laser pulse parameter after 5 s of heating cycle ending.

in this region. This is particularly true in the close region of the wall-free surface intersection of the melt pool. The Marangoni convection is also introduced in the simulations, which alters the particle positions at the surface because of the high Marangoni current in the vicinity of the melt free surface. In the case of pulse parameter $\beta=1$ (Fig. 7), mobility of the particles is low and only few particles are relocated at the free surface of the melt pool. This behavior is associated with the natural convection current, which remains low in the shallow melt pool because of small changes in the density. It should be noted that the absorption of the incident radiation also takes place in the melt pool while creating the temperature difference in the molten fluid during its formation. However, the amount of absorbed energy becomes less in the shallow melt pool while giving rise to attainment of a small temperature difference in the liquid layer. This in turn suppresses the intensity of the natural convection current. Marangoni flow is mainly governed by the surface tension gradient at the free surface, Marangoni current results in relocation of some of the hard particles from their original place. Fig. 9 shows particle distribution predicted and obtained from the experiment. The experimental data are presented in terms of scanning electron microscope (SEM) micrograph of the cross-section of the heated region. The hard particles appear as fine size bright colored spots in the

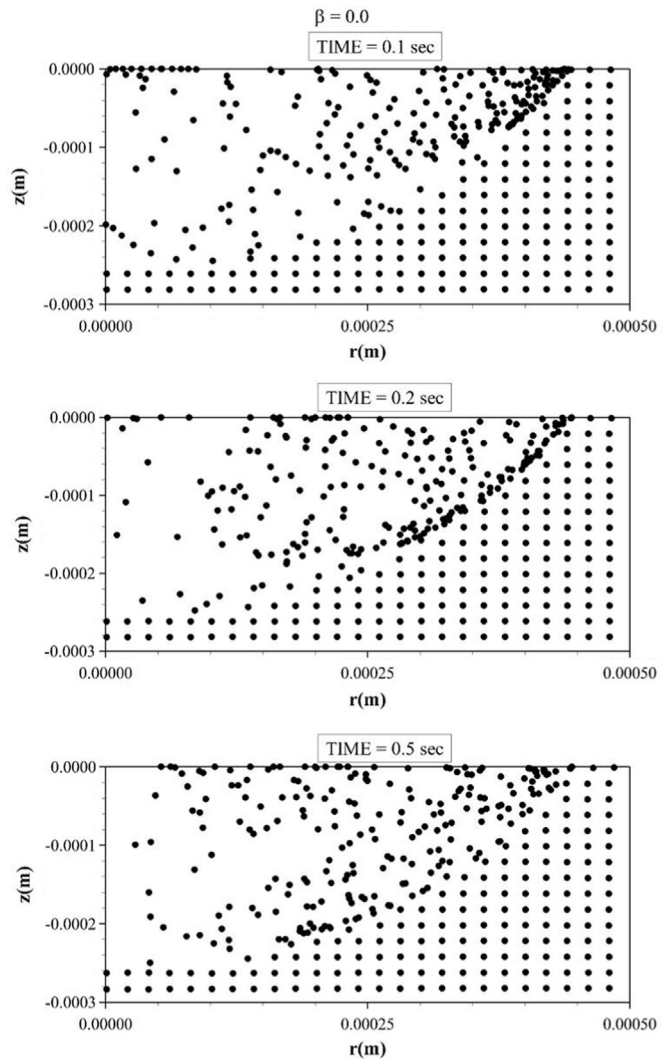


Fig. 8. WC particle distribution in the cross-section of laser irradiated region for laser pulse parameter $\beta=0$ and various periods in the cooling cycle.

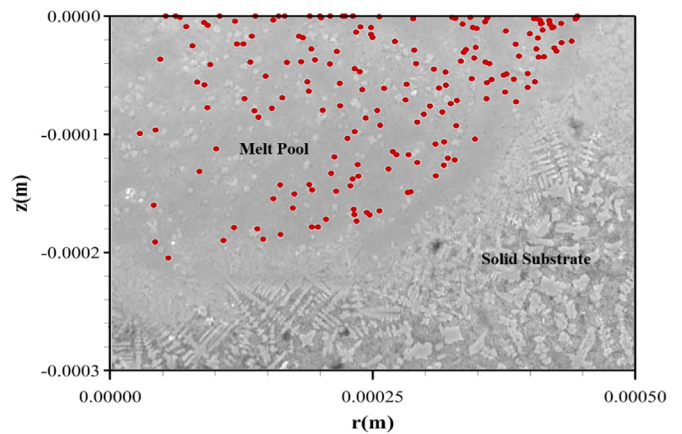


Fig. 9. SEM micrograph of cross-section of the laser treated layer and particle distribution predicted from the simulations. SEM micrograph and simulated section are overlaid. Laser pulse parameter $\beta=0$.

scanning electron micrograph. Streamlining of hard particles in the SEM micrograph is also evident, which agrees well with the predictions. In addition, particle relocation shows almost similar trend in the melt pool. However, some variations in the particle

distribution in the melt pool are attributed to the initial distribution of the hard particles across the cross-section inside the workpiece prior to the laser irradiation. In this case, the particles may not be distributed exactly uniform in the workpiece (Fig. 3).

Figs. 10 and 11 show the variation of the maximum temperature and the maximum velocity in the melt pool with the laser pulse parameter, respectively. The pulse parameter with small values results in high values of the maximum temperature and the maximum velocity in the melt pool. Consequently, the Gaussian distribution of the laser pulse intensity gives rise to the highest peak temperature and the maximum density variation in the melt pool. The large density variation is associated with the formation of the large melt pool depth. The increased in depth of the melt pool is also observed from Fig. 12, in which the depth of the melt pool variation with the laser pulse parameter. The similar situation is observed for the maximum flow velocity in the melt pool. Consequently, increasing melt pool depth results in increased melt flow velocity in the melt pool while modifying the particle

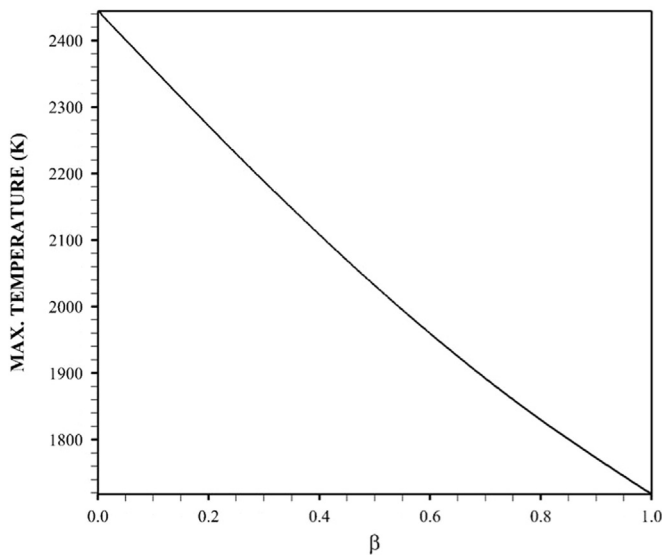


Fig. 10. Maximum temperature in the melt pool for various values of the laser pulse parameter.

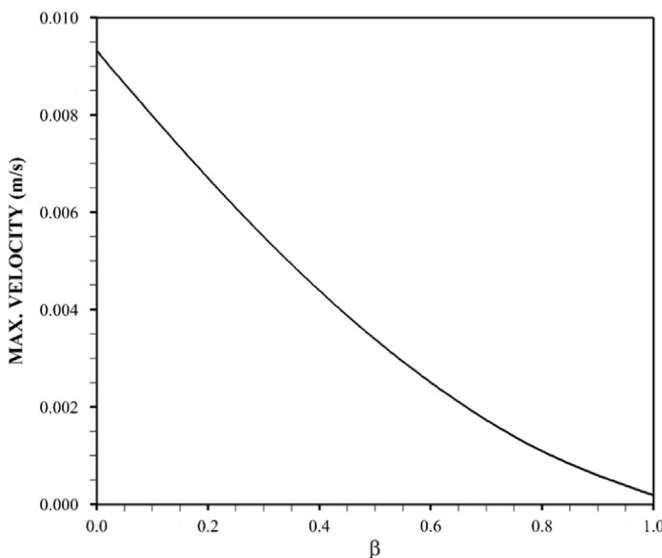


Fig. 11. Maximum flow velocity, due to natural convection and Marangoni currents, in the melt pool for various values of the laser pulse parameter.

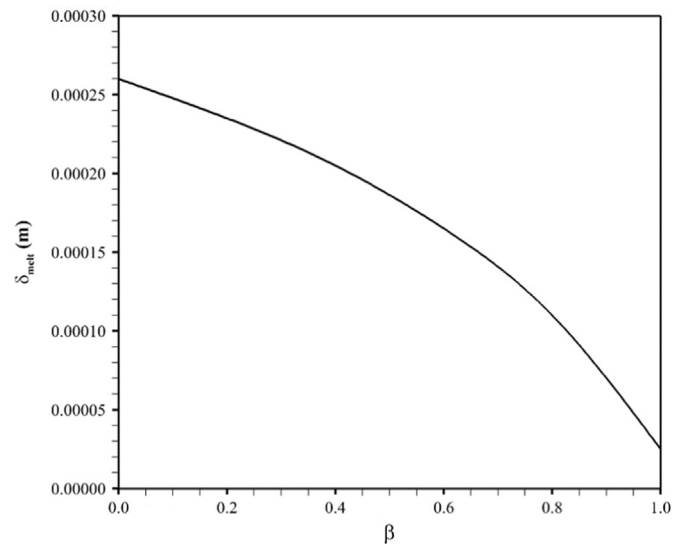


Fig. 12. The maximum depth of the melt pool for various values of the laser pulse parameter.

distribution in the melt pool. However, the functional behavior of the melt pool depth with laser pulse parameter is different than the behavior of the maximum temperature and the maximum velocity. This is because of the fact that the growth of the melt pool depends on the phase change of the substrate material. In addition, absorption of the incident radiation and the diffusional transport from surface towards the solid bulk at the melt pool interface govern the internal energy gain of the substrate material. Therefore, internal energy gain and the phase change demonstrate rather parabolic behavior than the linear so that the melt pool depth grows in a parabolic form with the laser pulse parameter.

Fig. 13 shows temporal variation of surface temperature at the irradiated spot center for various values of the laser pulse parameter. Temperature rises rapidly in the early heating period and attains almost steady values towards the end of the heating pulse. The rapid increase of temperature is associated with the internal energy gain by the substrate material from the irradiated laser field in the solid phase. This gives rise to the rapid rise of internal energy in the solid phase. However, as the time progresses, the phase change initiates and the phase change completes across the liquidus and solidus temperatures. As the heating period progresses further, sensible heating occurs in the liquid phase. Since the liquidus and solidus temperature of the substrate material are close and well below the maximum temperature at the surface (Table 1), melting takes place in a very short time at the irradiated surface. Therefore, sensible heating takes over the phase change at the surface for the large percentage of the heating cycle duration. As the time progresses, heat diffusion from the surface region towards the solid bulk increases due to the attainment of high temperature gradients in the surface vicinity. This suppresses temperature rise at the surface. In addition, sharp decay of temperature at the surface along the radial direction (Fig. 5) causes the development of the high temperature gradients in the radial direction. Consequently, surface temperature increase at the irradiated spot center is suppressed by the combination of the diffusional heat flux towards the solid bulk. This results in almost steady behavior of temperature increase with progressing time. The value of the maximum temperature changes with the laser pulse parameter; however, general behavior of surface temperature with time remains almost same for all the laser pulse parameters considered. Once the heating cycle ends, the cooling cycle is initiated at which surface temperature decays sharply in the early cooling cycle and temperature decay becomes gradual as the

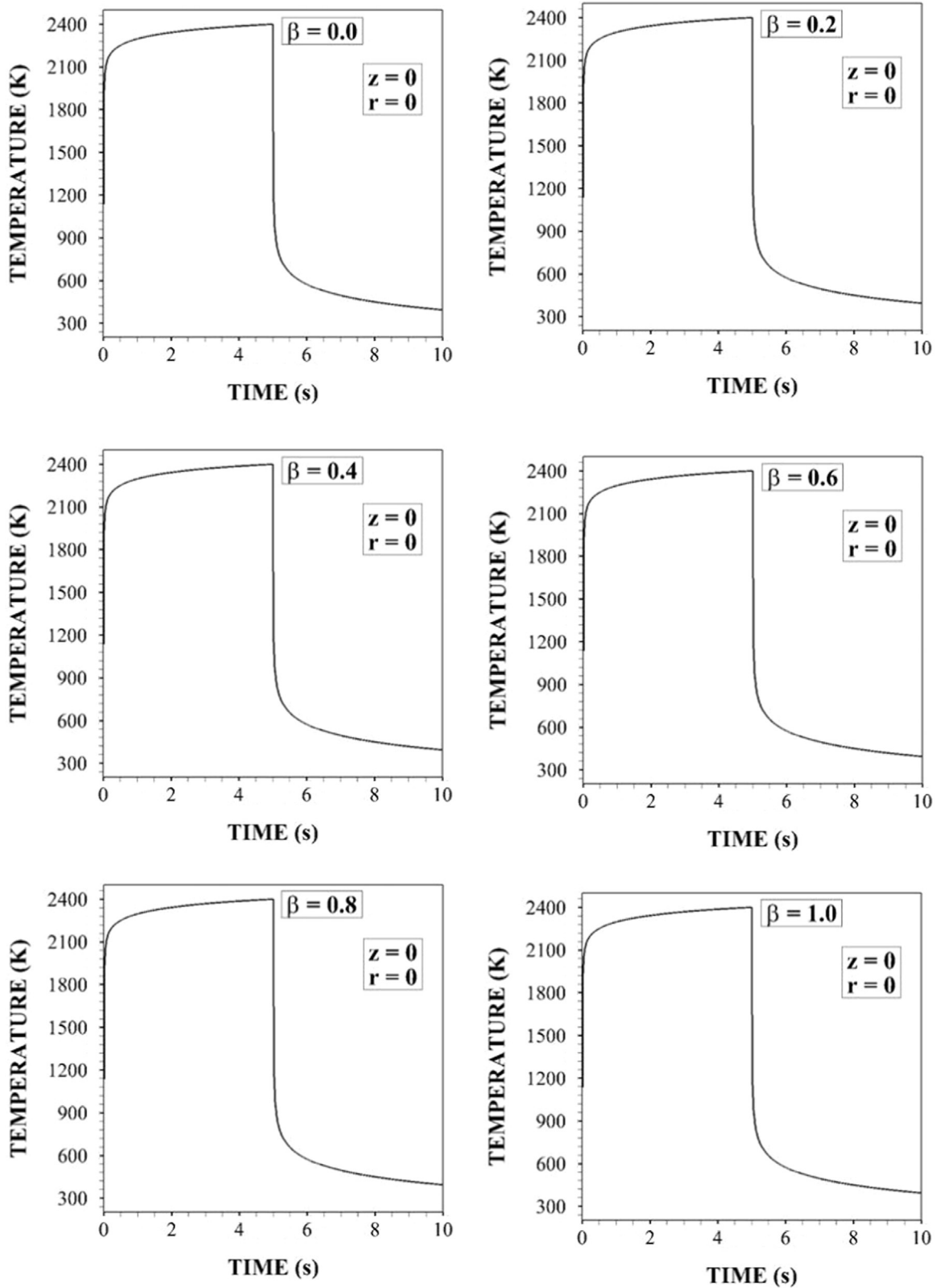


Fig. 13. Temporal variation of surface temperature at the irradiated spot center for various values of the laser pulse parameter.

cooling period progresses. The sharp decay of surface temperature indicates that heat diffusion from the irradiated spot center towards the solid bulk below the surface as well as in the radial direction reduces temperature at the spot center. This argument is true for all laser pulse parameters considered.

6. Conclusion

Laser pulse heating of steel substrate with presence of WC particles is carried out. Temperature field in the solution domain is predicted numerically incorporating the phase change in the

irradiated region. The effect of laser pulse parameter, which defines the laser pulse intensity distribution across the irradiated surface, on temperature field and melted zone structure is examined. An experiment is carried out to validate the predictions of surface temperature variation with time. In addition, laser melting experiments are carried out to observe the particle distribution in the melt pool. It is found that predictions of surface temperature agree well with the experimental data. The particles in the melt pool form streamline alignment close to the melt pool wall, which is in agreement with the predictions. The Gaussian pulse intensity distribution results in the maximum temperature in the irradiated region and the maximum velocity of the combination of the natural and Marangoni flow current in the melt pool. The displacement of WC particles is high in the free surface region of the melt pool where the Marangoni current is high. Since the shear layer in the vicinity of the melt pool wall gives rise to low flow velocities, WC particles almost sediment and agglomerate in this region. This situation is also observed from the experimental data. Increasing laser pulse parameter (β) reduces the peak power intensity at the irradiated spot center, which causes attainment of low surface temperature across the irradiated spot. In addition, lowering peak power intensity and expanding the intensity distribution at the irradiated surface gives rise to shallow melt depth, which is more pronounced for the laser parameter $\beta=1$. In this case, uniform like and shallow melt pool depth is resulted in the irradiated region. The location of WC particles remains almost the same in the melt pool, except at the melt pool surface where the Marangoni current remains high. Surface temperature at the irradiated spot center rises rapidly in the early heating period because of the internal energy gain from the irradiated field in the surface region. However, temperature rise becomes gradual as heating period progresses, which is associated with the heat diffusion from the irradiated surface towards the solid bulk increases with progressing time. This in turn suppresses temperature increase at the surface; in which case, steady rise of surface temperature is resulted until the laser pulse ends.

Acknowledgments

The authors acknowledge the support of King Fahd University of Petroleum and Minerals (Grant No. IN141001) Dhahran, Saudi

Arabia for this work.

References

- [1] H. Thomsen, H. Kahlert, M. Bonitz, J. Schablinski, D. Block, A. Piel, A. Melzer, Laser heating of finite two-dimensional dust clusters: B. Simulations, *Phys. Plasmas* 19 (2) (2012), <http://dx.doi.org/10.1063/1.368024>.
- [2] J. Zhang, D. Li, W. Fu, L. Zhao, Numerical simulation of multi-component powder in selective laser sintering, *Adv. Mater. Res.* 139–141 (2010) 630–633.
- [3] S.B. Mansoor, B.S. Yilbas, Laser short-pulse heating: influence of spatial distribution of absorption coefficient on temperature field in silicon film, *J. Laser Micro/Nanoeng.* 7 (2) (2012) 176–188.
- [4] O.B. Kovalev, A.V. Zaitsev, D. Novichenko, I. Smurov, Theoretical and experimental investigation of gas flows, powder transport and heating in coaxial laser direct metal deposition (DMD) process, *J. Therm. Spray Technol.* 20 (3) (2011) 465–478.
- [5] Y. Ioannou, C. Doumanidis, M.M. Fyrillas, K. Polychronopoulou, Analytical model for geometrical characteristics control of laser sintered surfaces, *Int. J. Nanomanuf.* 6 (1–4) (2010) 300–311.
- [6] D. Dai, D. Gu, Y. Li, G. Zhang, Q. Jia, Y. Shen, Numerical simulation of metallurgical behavior of melt pool during selective laser melting of W-Cu composite powder system, *Chin. J. Lasers* 40 (11) (2013), <http://dx.doi.org/10.3788/CJL201340.1103001>.
- [7] T. Amine, J.W. Newkirk, F. Liou, Numerical simulation of the thermal history multiple laser deposited layers, *Int. J. Adv. Manuf. Technol.* 73 (9–12) (2014) 1625–1631.
- [8] S. Wen, Y.C. Shin, Modeling of transport phenomena during the coaxial laser direct deposition process, *J. Appl. Phys.* 108 (4) (2010), <http://dx.doi.org/10.1063/1.3474655>.
- [9] K. Antony, N. Arivazhagan, K. Senthikumar, Numerical and experimental investigations on laser melting of stainless steel 316L metal powders, *J. Manuf. Process.* 16 (3) (2014) 345–355.
- [10] B.S. Yilbas, S.S. Akhtar, C. Karatas, K. Boran, Laser treatment of dual matrix cast iron with presence of WC particles at the surface: influence of self-annealing on stress fields, *Opt. Laser Technol.* 76 (2016) 6–18.
- [11] T. Kumpulainen, J. Pekkanen, J. Valkama, J. Laakso, R. Tuokko, M. Mäntysalo, Low temperature nanoparticle sintering with continuous wave and pulse lasers, *Opt. Laser Technol.* 43 (3) (2011) 570–576.
- [12] G.J. Li, J. Li, X. Luo, Effects of post-heat treatment on microstructure and properties of laser clad composite coatings on titanium alloy substrate, *Opt. Laser Technol.* 65 (2015) 66–75.
- [13] S. Liu, P. Farahmand, R. Kovacevic, Optical monitoring of high power direct diode laser cladding, *Opt. Laser Technol.* 64 (2014) 363–376.
- [14] V.R. Voller, C. Prakash, A fixed-grid numerical modeling methodology for convection-diffusion mushy region phase-change problems, *Int. J. Heat Mass Transf.* 30 (1987) 1709–1720.
- [15] S.Z. Shuja, B.S. Yilbas, Pulsative heating of surfaces, *Int. J. Heat Mass Transf.* 41 (1998) 3899–3918.
- [16] H. Tanerolu, N. Akar, V. Kiliçli, Examination of microstructure and mechanical properties of al2024 alloy produced by thixocasting, *J. Fac. Eng. Archit. Gazi Univ.* 28 (4) (2013) 803–809.